Acta Materialia 242 (2023) 118478

Contents lists available at ScienceDirect

Acta Materialia

journal homepage: www.elsevier.com/locate/actamat

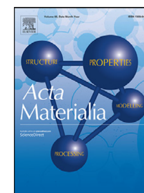

Full length article

Strategic texturation of VO_2 thin films for tuning mechanical, structural, and electronic couplings during metal-insulator transitions

Yuwei Zhang [a,b], Cole D. Fincher [a], Rebeca M. Gurrola [b], Wilson Serem [c], Dexin Zhao [b], Jungho Shin [a], Sarbajit Banerjee [b,d], Kelvin Xie [b], Patrick Shamberger [b], Matt Pharr [a,*]

[a] Department of Mechanical Engineering, Texas A&M University, College Station, TX 77840, USA
[b] Department of Material Science and Engineering, Texas A&M University, College Station, TX 77840, USA
[c] Materials Characterization Facility, Texas A&M University, College Station, TX 77843, USA
[d] Department of Chemistry, Texas A&M University, College Station, TX 77840, USA

ARTICLE INFO

Article history:
Received 25 March 2022
Revised 1 October 2022
Accepted 23 October 2022
Available online 26 October 2022

Keywords:
VO_2
Metal-insulator transitions
Crystal structure
Anisotropic deformation
Fracture mechanics
Neuromorphic computing

ABSTRACT

Owing to its pronounced metal-insulator transition at ~340 K, vanadium dioxide (VO_2) has emerged as a promising candidate material to emulate neuronal logic and memory functions for neuromorphic computing applications. For viable implementation into practical devices, it is critical to understand the fundamental mechanical behavior of VO_2 during this phase transformation. Herein, we implemented sputter deposition under various conditions to strategically texture VO_2 thin films, thereby enabling us to examine the influence of crystal orientation on mechanical, structural, and electrical properties across its characteristic metal-insulator transition. Notably, polycrystalline VO_2 and epitaxial VO_2/sapphire (0001) films developed tension, whereas epitaxial VO_2/TiO_2 (001) developed compression in heating through the phase transformation. Through structural analysis, we attribute this tension/compression disparity to highly anisotropic deformation that occurs during the phase transformation. Corresponding analyses from linear elastic fracture mechanics enable the prediction of a critical film thickness, below which polycrystalline VO_2 films will not fracture, which has implications for the design of resilient neuromorphic architectures. Similarly, by analyzing the stress evolution in epitaxial VO_2/TiO_2 (001) films, we find that fracture occurs during sputter deposition itself. Finally, we conduct simultaneous measurements of mechanical stress and electrical conductance of polycrystalline and epitaxial VO_2 thin films during thermal cycling. Surprisingly, we unveiled that the orientation of the film can even alter the temperature-sequence of the macroscopic electrical response and overall stress response during the phase transformation, which we attribute to spatial heterogeneities in the transformation.

© 2022 Acta Materialia Inc. Published by Elsevier Ltd. All rights reserved.

1. Introduction

Electron-correlated transition metal oxides exhibiting pronounced metal-insulator transitions (MITs) are excellent candidates to emulate the spiking behavior of biological neurons. VO_2 undergoes a first-order diffusionless and hysteretic transition from a high-symmetry rutile R phase to a low-symmetry stable monoclinic M_1 (or metastable monoclinic M_2 or M_3) phase at ~340 K [1–5]. Stemming from this behavior, Yi et al. demonstrated 23 types of biological neuronal behaviors through two-channel devices of VO_2 as active memristors [6]. Much attention has focused on tuning the transition temperature, e.g., by adding dopants, tuning epitaxial matching to substrates, and changing film thickness [7–10]. Still, given the change in crystal symmetry and anisotropic strains accompanying the structural transition, VO_2 often suffers severe mechanical deformation during thermal cycling [11–17]. For instance, Nagashima et al. have reported fracture of epitaxial VO_2 thin films on TiO_2 (001) substrates [16]. Additionally, Muraoka et al. found that VO_2 thin films deposited on TiO_2 (001) and TiO_2 (110) substrates displayed a wide transition temperature range. They were able to tune the transition temperature through substrate-induced mismatch strain [18]. Implementation of VO_2 into devices of practical utility requires a comprehensive understanding of its mechanical behavior, as to ensure stability and durability across extended current-, voltage-, or thermally-driven electronic transitions.

For instance, it is important to determine stress levels that develop in physically constrained environments during the metal-insulator transitions, as to guide the design of practical devices that avert damage during operation. Viswanath et al. reported re-

* Corresponding author.
E-mail address: m-pharr@tamu.edu (M. Pharr).

https://doi.org/10.1016/j.actamat.2022.118478
1359-6454/© 2022 Acta Materialia Inc. Published by Elsevier Ltd. All rights reserved.

versible stress evolution of polycrystalline VO_2 thin films over 100 thermal cycles through the metal-insulator transition [19]. They also investigated the stress evolution behavior during incomplete martensitic transformations and the corresponding stress relaxation during the phase transformation [19]. Balakrishnan et al. later observed twinning near cracks that formed during the phase transformation of VO_2 on Si_3N_4 membranes, suggesting crack-induced plasticity during the transition [20]. In both studies, the authors found that tensile stresses developed in polycrystalline VO_2 upon heating through the phase transformation. However, the origin of these tensile stresses [21,22] is unclear, given that volumetric expansion occurs during the phase transformation, which would thus seem likely to induce compressive stresses when constrained by surrounding materials. Moreover, stresses that develop during MITs in epitaxial films of VO_2 remain unknown.

In terms of fracture behavior, several studies have observed cracking in epitaxial VO_2 [12,13,15–17,23–25]. In VO_2 $(40\bar{2})_M$ on TiO_2 (001), Nagashima et al. experimentally observed a critical thickness of VO_2 of 15 nm above which the film fractured [16]. Rodriguez et al. observed that the crack density increases with film thickness in the same system [15]. Paik et al. attributed their observed decrease in on/off ratio (in resistivity across the MIT) to stress relaxation associated with cracking in VO_2 $(40\bar{2})_M/TiO_2$ (001) [17]. One possibility was proposed by Nagashima and Krisponeit, who speculated that VO_2 $(40\bar{2})_M$ $/TiO_2$ (001) fractures during the MIT upon cooling by comparing the thermal expansion coefficients of VO_2 films and TiO_2 (001) substrates before and after the MIT transition using pre-existing data [16,24]**.** Here, we have sought to delineate critical attributes of VO_2 thin films, formulated in terms of lattice compatibility with the substrate and film thickness, that are necessary to ensure damage-free operation across the characteristic metal—insulator transition of VO_2

Beyond these mechanical studies, several studies have provided insight into the effects of epitaxy on the phase transformation and corresponding electrical properties during the MIT in VO_2. For instance, in a series of studies, Liu et al. found phase separation into unidirectionally-oriented metallic stripes in VO_2 deposited on TiO_2 (100) and TiO_2 (110) substrates [26–28], but the same group found no stripe-like patterns in VO_2 deposited on TiO_2 (001) [14]. Qazilbash et al. observed nanoscale metallic puddles at the onset of the MIT in polycrystalline VO_2 [29]. Overall, it is important to fully understand the interplay among mechanical stresses/strains, crystal orientation, electric properties, temperature, and phase transformations in these systems.

To address the gaps in knowledge outlined above, herein we fabricated polycrystalline $VO_2/SiO_2/Si$ (100), epitaxial VO_2 $(020)_M/TiO_2$ (001), and epitaxial VO_2 $(\bar{4}02)_M$/sapphire (0001). We utilized a multi-beam optical stress sensor (MOS) technique to measure the evolution of stresses during the MIT in these films. Highly anisotropic stresses occurred in these systems, which we rationalize by analyzing the crystal structure and corresponding deformation behavior in these systems. To better understand the effect of the crystal structure on the temperature sequence of the macroscopic electrical response and overall stress response of the thin film, we conducted simultaneous measurements of mechanical stresses and electrical conductance during the phase transformation of polycrystalline VO_2 and epitaxial VO_2 $(020)_M$ thin films. We found that the orientation of the film can alter the temperature sequence of the macroscopic electrical response and overall stress response through complementary characterization. We also experimentally characterized and analyzed fracture behavior in these systems. Namely, as informed by our measurements of mechanical properties and accumulated stresses during a thermal cycle, we implemented an analysis from fracture mechanics to predict a critical film thickness of polycrystalline VO_2 thin films, below which fracture will not occur. We compared these predictions to experimental observations by thermal cycling VO_2 films of varying thickness while simultaneously monitoring damage. Similarly, we analyzed the root cause of fracture of epitaxial VO_2 $(40\bar{2})_M/TiO_2$ (001) thin films and found that damage in these systems likely stems from the fabrication process itself, i.e., during deposition at high temperatures. Overall, these comprehensive mechanical studies provide insight into the design of mechanically robust VO_2 devices, e.g., for applications in neuromorphic computing devices.

2. Experimental

2.1. Synthesis of VO_2 thin films

We utilized two side mirror-polished silicon (100) wafers with 150 nm of thermal oxide (SiO_2) on top (University Wafer), sapphire (0001), TiO_2 (001), and TEM grids with 18 nm-thick SiO_2 support films as our substrates. The substrates (barring the TEM grid) were cleaned with acetone and 2-propanol and placed into a sputtering system (AJA Inc.) with a base pressure of $\sim 5 \times 10^{-8}$ Torr. All depositions utilized a metal vanadium target, a working pressure of 2.0 mTorr, a mixture of argon and oxygen gas (Ar: 20 sccm, O_2: 4.1 sccm), a DC power of 200 W, a substrate rotation of 40 rpm, and a substrate temperature of 600ºC. The deposition temperature and time is chosen to meet the needs of both electrical performance (e.g., reasonably good on/off ratios) and consistency among three different substrates, i.e., as to not conflate too many variables when comparing among different substrate systems. 30 min of deposition produced 150 nm, 60 nm, and 90 nm films of VO_2 on SiO_2/Si (100), sapphire (0001), and TiO_2 (001), respectively. By controlling the deposition time, we also produced films on SiO_2/Si (100) wafers of varying thickness – 387 nm(1 h), 698 nm (2 h), and 1630 nm (3 h) – to study the effects of film thickness on performance, e.g., in terms of fracture behavior. Immediately following deposition, we annealed each sample in the sputtering chamber without breaking vacuum at 600 °C for 3 h. We note here that our deposition conditions did not result in a linear increase in film thickness with deposition time. As such, to ensure accuracy in our findings and calculations herein, we measured the thickness of each film individually after deposition. We measured the film thickness of polycrystalline specimens by milling a trench through the thickness of as-prepared samples using a focused ion beam (FIB) inside a scanning electron microscope (SEM, Tescan LYRA-3 Model). We measured the film thickness of epitaxial VO_2/TiO_2 (001) and VO_2/sapphire (0001) through transmission electron microscopy (TEM).

2.2. Structural and morphological characterization

A parallel beam geometry using a Bruker-AXS D8 X-ray diffractometer with a Cu Kα (wavelength $\lambda = 0.154$ nm) radiation source and a parabolic Göbel Mirror produced X-ray diffraction patterns. A scanning electron microscope (SEM, JEOL JSM-7500F) operating at 10 kV captured the surface morphology. An atomic force microscope (AFM, Bruker-Dimension Icon) determined the morphology and roughness of the surface of the film. A DXS 500 optical microscope captured images of the surfaces of samples during thermal cycling to monitor the evolution of damage. The crystal structures of VO_2 with a specific orientation are generated with Vesta [30–32].

2.3. Mechanical characterization

A multibeam optical stress sensor (MOS) from k-Space Associates monitored the curvature of the substrates (ΔK) during thermal cycling (e.g., from 40 to 200 ºC). The experimental setup is shown in the Fig. 1d. We spread thermal paste on a heating stage

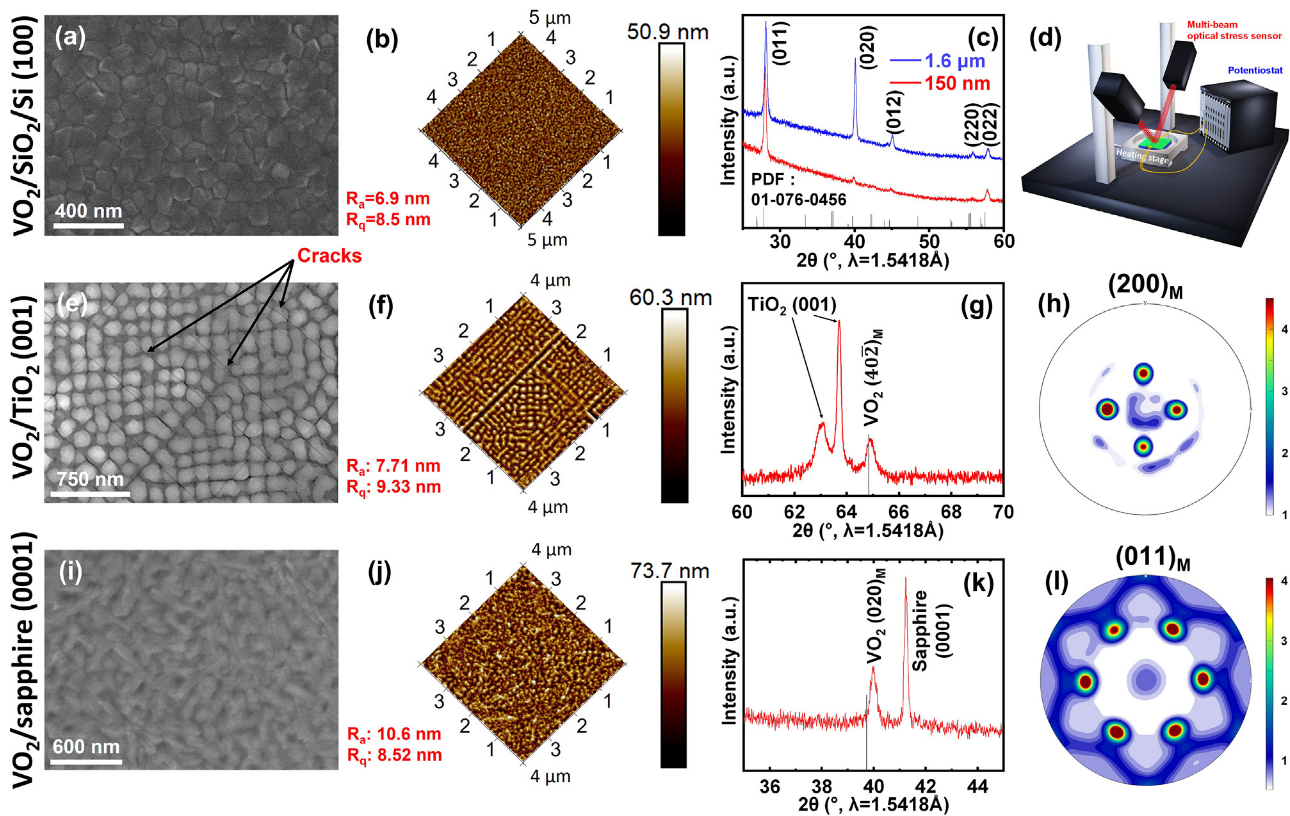

Fig. 1. Surface morphology and crystal structure characterization of as-deposited VO_2 thin films on SiO_2/Si (100) (first row), TiO_2 (001) (second row), and sapphire (0001) (third row) – (a), (e), and (i): SEM images, (b), (f), and (j): AFM images, (c), (g), and (k): x-ray diffraction patterns, (h) and (l): XRD pole figure, and (d) experimental set up for simultaneous mechanical stress and electrical characterization during thermal cycling.

(TMS 94, Linkam Scientific Instruments Ltd.) prior to mounting the sample, as to enhance heat conduction. Using Stoney's equation, we deduced the average in-plane stresses in the thin film during thermal cycling [33–35]:

$$\Delta\sigma = \frac{M_s h_s^2}{6h_f}\Delta K \quad (4)$$

where M_s is the biaxial modulus of the substrate ($M_{SiO_2/silicon(100)} = \frac{1}{s_{11}+s_{12}} = 180$ GPa [36–39], $M_{sapphire\ (0001)} = \frac{1}{s_{11}+s_{12}} = 578$ GPa [39–41], $M_{TiO_2\ (001)} = \frac{1}{s_{11}+s_{12}} = 360$ GPa [39,42,43]), h_s is the thickness of the substrate ($h_{SiO_2/Silicon(100)} = 325\mu m$, $h_{sapphire\ (0001)} = 100\ \mu m$, $h_{TiO_2\ (001)} = 500\ \mu m$), and h_f is the thickness of the VO_2 film. In this study, the stress $\Delta\sigma$ represents the change in the average in-plane engineering stress. Any expansion or contraction out of plane will not contribute to the stress measurement. We use the sign convention of tensile stress as being positive and compressive stress as being negative.

Stoney's equation assumes that the deformation of the thin film is axisymmetric [37]. In the case of textured polycrystalline VO_2/SiO_2/Si (100), the grains are randomly oriented in-plane, even though the out-of-plane orientation is highly textured Diffraction patterns of the epitaxial VO_2/TiO_2 (001) and VO_2/sapphire (0001) films contain 4-fold and 6-fold in-plane symmetry, respectively, as shown in Fig. 1h and 1l. The diffraction spots in the VO_2/TiO_2 (001) film reflect an epitaxial relationship between the VO_2 film and the underlying TiO_2 (001) substrate, which has 4-fold symmetry. While the symmetry of the VO_2 crystal structure is reduced when it transforms to the monoclinic phase, the film retains the 4-fold symmetry of the underlying TiO_2 substrate. In the latter case, the polycrystalline growth of epitaxial VO_2 on sapphire occurs in 3 symmetrically equivalent rotational domains, resulting in a superposition in a diffraction pattern with 6-fold symmetry. In fact, the films we fabricated are highly epitaxial but are not identically single crystals as shown in Fig. 1e and Fig. 1i. The small in-plane misorientation as indicated in the pole figures (Fig. 1h and 1l) induces some randomness (i.e., isotropy) in the in-plane directions. As such, the epitaxial VO_2/TiO_2 (001) and VO_2/sapphire (0001) films are in-plane axisymmetric, at least to the first order. Furthermore, Huang et al. calculated that hexagonal (00*l*) plane, tetragonal (00*l*), and cubic (00*l*) and (*hhh*) planes are equivalently in-plane isotropic, which thus implies that the deformation of the substrates in our study are subjected to the macroscopically homogeneous equiaxial stress [39]. On a related note, the MOS system can track the curvature along two orthogonal directions (X and Y). Fig. S7 indicates a relatively small difference in the measured curvatures along these two directions in all of our films. The small difference in the curvatures between the two perpendicular directions is possibly due to the variation in the thickness of the deposited film or slightly non-uniform heat flux across the samples [44].

2.4. Electrical characterization

We used Elform Heat Seal Connectors (Elform Inc.) to connect the films to a potentiostat. Using a PARSTAT MC Multichannel Potentiostat (Princeton Applied Research), we conducted electrical conductance measurements under a constant voltage (0.02 V).

2.5. Nanoindentation

We measured mechanical properties with a Nanomechanics Nanoflip indentation system operated in a temperature chamber.

Specimens from Si wafers (only) as well as specimens from polycrystalline VO_2 films sputtered onto Si wafers were mounted using cyanoacrylate adhesive prior to indentation. All measurements of hardness, *H*, and elastic modulus, *E*, were performed with a Berkovich triangular pyramid indenter using the continuous stiffness measurement technique (CSM) with a target dynamic root-mean-square amplitude of 2 nm and loading rate by load ($\dot{P}/P$) value of 0.05 s^{-1}. The tip area function was calibrated based on fused silica at indentation depths between 100 and 450 nm. The machine frame stiffness was calculated based on indentation of a reference Si substrate at the same temperatures of the relevant measurements. Holding the indenter tip against the sample and measuring the displacement versus time enabled assessment of thermal equilibrium for the tip and sample. All indentation measurements were taken only after the thermal drift was measured as less than 0.05 nm/s. Hardness and apparent elastic modulus values were calculated using the Oliver—Pharr approach [45]. The elastic modulus of the VO_2 film on the Si substrate was calculated based upon the Hay—Crawford thin film model [46]. To this end, the Si substrate's elastic modulus versus depth was measured directly over 50 individual tests, with the average elastic modulus interpolated at 5 nm increments in depth. This elastic modulus of the substrate as a function of the depth was then utilized in calculating the elastic modulus of the VO_2 film as a function of the depth using the Hay-Crawford model, adopting a film thickness of 1.63 μm, as measured from FIB cross-sectional images, and a Poisson's ratio of the film and substrate of ν =0.2 [46]. This technique was applied independently at 25 °C and 85 °C.

3. Results

Fig. 1 shows the surface morphology and crystal structure of sputter-deposited polycrystalline and epitaxial VO_2 thin films. Fig. 1a and 1b show the surface morphology of a 1.63 μm-thick film and indicate a grain size of approximately 120 nm. Fig. S1 shows similar morphologies in polycrystalline VO_2 thin films of two other film thickness: 387 nm and 698 nm. Fig. S2 shows further details of a 150-nm thick polycrystalline VO_2 thin film through TEM studies. Fig. 1e and 1f show that epitaxial VO_2 films deposited on TiO_2 (001) demonstrate a near regular square island-type morphology with large cracks. By contrast, Fig. 1i and j show that epitaxial VO_2 films deposited on sapphire (0001) demonstrate no such notable features. Fig. S3 displays differences in surface morphology between VO_2/TiO_2 (001) and VO_2/sapphire (0001) on several samples using optical microscopy. Fig. S4 shows the cross section of a VO_2 thin film deposited on TiO_2 (001) substrate from transmission electron microscopy. The VO_2/TiO_2 interface appears that it may be somewhat diffuse, as shown in Fig. S4. One possible reason is the Z number between Ti and V elements are similar so it is difficult to distinguish between them with our given microscopy technique, i.e., this appearance may be an imagining artifact. Still, we cannot completely rule out the possibility of a diffusive solid solution layer of $Ti_xV_{1\text{-}x}O_2$ existing between the film and the substrate. However, a stepwise metal insulator transition phenomenon would likely occur if such an intermetallic compound existed in our VO_2/TiO_2 thin films, as has been seen in previous work [18]. As such, we surmise that an intermetallic compound ($Ti_xV_{1\text{-}x}O_2$) did not form with our synthesis conditions or that such a layer had a negligible effect on performance, as based on the results in Fig. 4e. In terms of roughness, the AFM scans over a few square microns indicate R_q values of 8.5 nm for polycrystalline VO_2/SiO_2/Si (100), 9.33 nm for VO_2/TiO_2 (001), and 8.52 nm for VO_2/sapphire (0001) (Fig. 1). These roughness values are approximately one order of magnitude smaller than the total film thicknesses, which thereby helps to ensure that Stoney's Equation (mentioned in Materials and Methods) is valid without any required modification and also helps in ensuring meaningful nanoindentation measurements at our reported indentation depths [37]. Fig. 1d shows an experimental setup that we implemented in this study.

Fig. 1 also presents x-ray diffraction data from these films. Fig. 1c shows diffraction patterns of both a 1.63 μm-thick and a 150 nm-thick VO_2 thin film, both of which indicate the polycrystalline nature of the samples deposited on SiO_2/Si (100). For the thinner film, the VO_2 $(011)_M$ reflection became more dominant relative to the (020) reflection, thereby indicating a more significant preferred texture in the thinner film. Fig. 1g shows a diffraction pattern from VO_2 deposited on TiO_2 (001), which indicates the epitaxial nature of the film, with the VO_2 $(\bar{4}02)_M$ plane as the sole reflection. Fig. 1k shows a diffraction pattern from VO_2 deposited on sapphire (0001), which indicates the epitaxial nature of the film, with the VO_2 $(020)_M$ plane as the sole reflection. The vertical black lines in all three figures show the powder diffraction pattern of VO_2-M_1 with PDF number: 01-076-0456. Fig. 1h and 1l show XRD pole figures of VO_2 $(40\bar{2})_M/TiO_2$ (001) and VO_2 $(020)_M$/sapphire (0001). VO_2 $(40\bar{2})_M/TiO_2$ (001) displays 4-fold symmetry diffraction patterns indicating a highly epitaxial film grown on a substrate with underlying 4-fold symmetry. In contrast, VO_2 $(020)_M$/sapphire (0001) exhibits 6-fold symmetry diffraction patterns, thus evidencing the existence of a polycrystalline textured VO_2 film with 3 symmetrically equivalent rotational domains in distinct orientations that mirror the underlying 6-fold symmetry of the sapphire substrate.

Fig. 2 displays the elastic modulus and hardness of a 1.6 μm-thick polycrystalline VO_2 film as a function of the indenter depth from nanoindentation studies. At an indentation depth of 150 nm, the elastic modulus is 224.4 ± 20.0 GPa at 25 °C and 210.4 ± 15.5 GPa at 85 °C. An unpaired *t*-test gives a p-value of 0.0048, meaning that despite the error bars appearing similar in magnitude to the difference between the mean values for the two temperatures, the modulus is indeed statistically significantly different for the two sample sets, reflecting the change in phonon dispersion as a function of temperature.

Indentation hardness measurements at 150 nm depth yielded values of 12.8 ± 2.0 GPa at 25 °C and 11.6 ± 1.5 GPa at 85 °C. An unpaired *t*-test for this data produces a p-value of 0.0084, again indicating that this data is statistically distinct. Given that the moduli for the VO_2_M thin film (~220 GPa) and silicon substrate (~195 GPa) are similar, and that Si's hardness was measured as near 13.5 GPa, we can reasonably assert that the apparent hardness represents that of the film itself within 5% accuracy [47]. The measurements provide direct experimental validation for softening of phonons in the tetragonal phase, as has been predicted by *ab initio* calculations and inferred from neutron scattering measurements; the observed softening is a consequence of soft anharmonic phonons, which are directly implicated in the increase of entropy that underpins stabilization of the metallic phase [48].

Fig. 3 shows that the fracture behavior of the VO_2 thin films is strongly influenced by the film thickness and the crystal orientation of the films. The top view image of a 1.63 μm-thick VO_2/SiO_2/Si (100) thin film indicates that the film fracture is predominately intergranular as indicated in Fig. 3a. Fig. 3b reveals both the fracture of a 1.63 μm-thick VO_2/SiO_2/Si (100) film and the delamination between the VO_2 film and the underlying substrate in the damaged regions. Videos S1-S4 show additional details of the morphological evolution of a 1.63 μm-thick VO_2/SiO_2/Si (100) thin film during heating and cooling. Fig. 3c and 3d display the top-view and cross-sectional morphology of a 698 nm-thick VO_2/SiO_2/Si (100) film after one thermal cycle. Fig. S1g, h reveal the surface morphology of thinner films (387 nm) after the first thermal cycle, and Fig. 5d shows the surface morphology of a 150 nm-thick film after 50 thermal cycles. Thinner polycrystalline films remain mechanically intact during fabrication and thermal

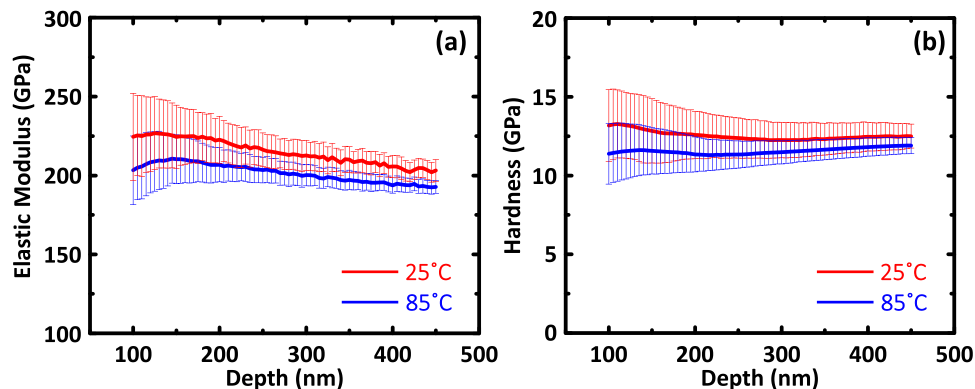

Fig. 2. Nanoindentation tests of 1.63 μm-thick polycrystalline VO_2 at 25 °C and 85 °C: (a) the elastic modulus and (b) the hardness as a function of indentation depth. The curves show the average of 16 and 50 tests at 25 °C and 85 °C, respectively, and the error bars represent the standard deviation.

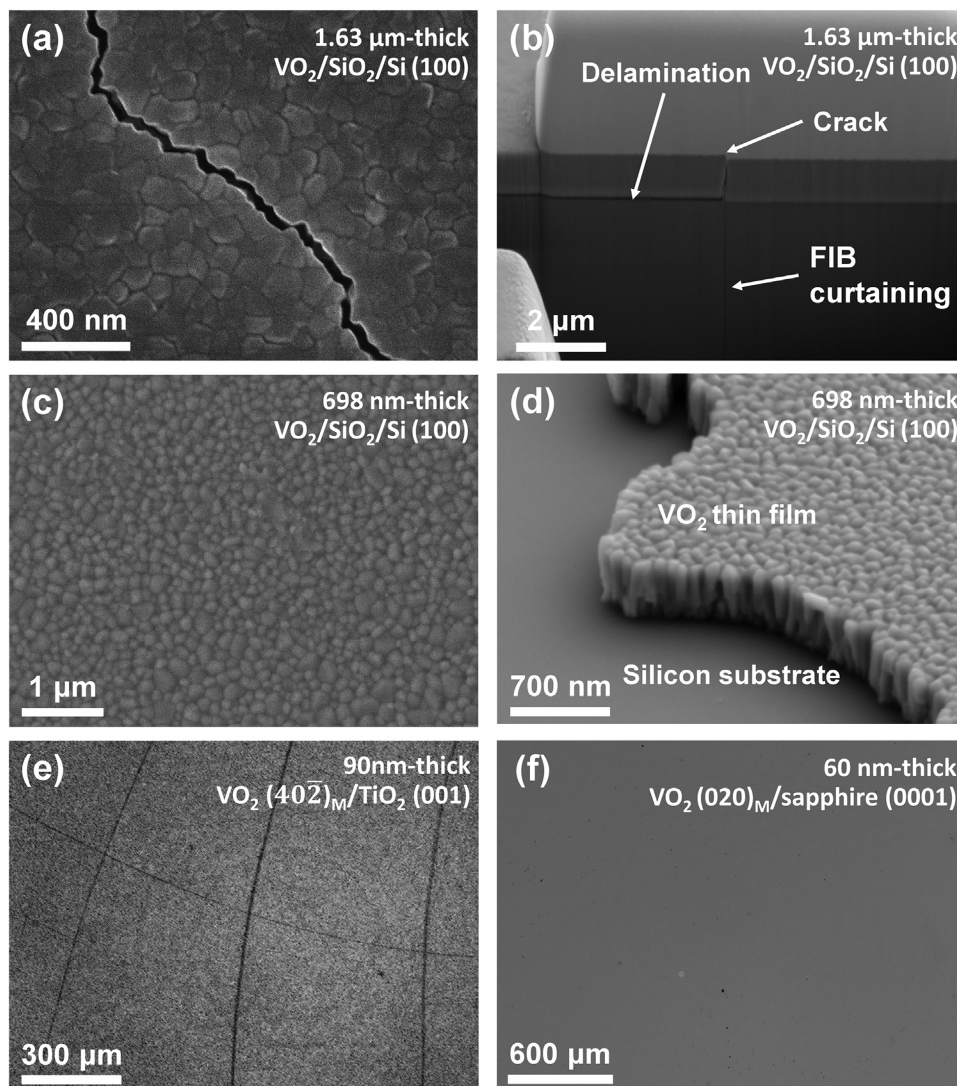

Fig. 3. (a) and (b) show fracture behavior of a 1.63 μm-thick polycrystalline VO_2 thin film deposited on SiO_2/Si (100) from the top-view and cross-sectional view after one thermal cycle. (c)&(d) show the absence of fracture of a 698 nm-thick polycrystalline VO_2 thin film deposited on SiO_2/Si (100) from the top-view and cross-sectional view after 5 thermal cycles. (e)&(f) show a top-view morphology of VO_2/TiO_2 (001) using an optical microscope illustrating cracking even before thermal cycling. (f) shows the absence of fracture of VO_2/sapphire (0001) using an optical microscope from the top-view morphology after 5 thermal cycles.

cycling. Fig. 3e shows the surface morphology of VO_2/TiO_2 (001) immediately after sputter deposition using an optical microscope. Cracks had already developed in these films even before any thermal cycling. Fig. 3f shows the surface morphology of VO_2/sapphire (0001) after 5 thermal cycles using an optical microscope. We observed no cracking behavior in this thin film even after 5 thermal cycles. Fig. S3 displays three additional optical microscope images of VO_2/sapphire (0001) and VO_2/TiO_2 (001) before and after 5 thermal cycles between room temperature and 90 °C. All the substrates were free from scratches/cracks before we transferred them into the sputtering chamber. These observations highlight the importance of the film thickness and the orientation of the thin films in maintaining mechanically integrity of the VO_2 thin films.

Fig. 4 shows measurements of stress in VO_2 thin films deposited on three different substrates while thermally cycling through their metal-insulator transition. To reiterate, the stress presented here represents the changes in stress relative to a reference stress, which we take as the stress at the beginning of the first thermal cycle. A similar method has been adopted in previous studies [33–35]. In Fig. 4a, we performed cooling tests of these three types of films from 200 to 100 °C to investigate thermal mismatch behavior at larger temperatures. Polycrystalline $VO_2/SiO_2/Si$ (100) and epitaxial VO_2 $(020)_M$/sapphire (0001) develop relative tension, whereas VO_2 $(40\bar{2})_M$ $/TiO_2$ (001) develop relative compression during cooling from 200 to 100 °C. The TiO_2 (001) plane has a larger relative thermal expansion coefficient than VO_2, as compared with the other two substrates (sapphire and silicon) which produces larger (negative) stress during cooling over this range [22,49,50].

Fig. 4b shows that the high temperature rutile phase VO_2-R ($P4_2/mnm$) has a singular V—V bond distance (d_1=2.851 Å) in contrast with the low temperature monoclinic phase VO_2-M ($P2_1/c$), which has alternating dimerized V—V chains (d_2=3.124 Å and d_1=2.654 Å) [3]. During heating through the phase transition, the volume expansion has been reported as 0.044% [21,22]. To better explain the stress evolution history in Fig. 4c, e and g, we present the areal change of the corresponding plane (the in-plane direction of the film) in Fig. 4d, f, and h next to the stress evolution behavior.

Fig. 4c shows that upon heating from 20 to 65 °C, small compressive stresses are generated in a 150 nm-thick polycrystalline $VO_2/SiO_2/Si$ (100) film due to the thermal mismatch of VO_2 and the Si substrate [21,51]. Upon further heating, significant tensile stresses (around 225 MPa) build up in heating from 65 to 80 °C through the metal-insulator transition. Upon completion of the phase transformation (above ∼80 °C), the thermal mismatch between VO_2 and the Si substrate again produces small compressive stresses. The stress evolution during cooling shows a similar trend, albeit with the metal-insulator transition temperature during cooling being located at a lower temperature range by ∼10 °C relative to that of heating. The stress accumulation during the phase transformation is approximately 225 MPa.

Epitaxial VO_2 $(020)_M$/sapphire (0001) displayed a similar trend to polycrystalline $VO_2/SiO_2/Si$ (100) in its stress evolution with some small numerical differences, as indicated in Fig. 4g, which may be related to the anisotropy of the elastic moduli of VO_2. The stress developed in heating epitaxial VO_2 $(020)_M$/sapphire (0001) to 65 °C is somewhat smaller compared with polycrystalline $VO_2/SiO_2/Si$ (100). Upon further heating, significant tensile stresses (around 280 MPa) build up in heating from 65 to 80 °C through the metal-insulator transition. The stress evolution during cooling shows a similar trend to heating, albeit with the metal-insulator transition temperature during cooling being located at a lower temperature range by ∼6 °C relative to that of heating. Overall, the tensile stresses in epitaxial VO_2 $(020)_M$/sapphire (0001) are nearly identical compared with polycrystalline VO_2 $(020)_M/SiO_2/Si$ (100), but epitaxial VO_2 $(020)_M$/sapphire (0001) displayed smaller temperature hysteresis between heating and cooling.

By contrast, VO_2 $(40\bar{2})_M/TiO_2$ (001) demonstrates vastly different mechanical behavior in heating through its metal-insulator transition. Remarkably, Fig. 4e shows that VO_2 $(40\bar{2})_M/TiO_2$ (001) develops relatively large compressive stresses (around −1100 MPa) during heating from 40 to 100 °C through the metal-insulator transition. Also, the temperature range of phase transformation is significantly larger than both $VO_2/SiO_2/Si$ (100) and VO_2 $(020)_M$/sapphire (0001). The stress evolution during cooling shows a similar trend to heating, albeit with the metal-insulator transition temperature during cooling being located at a lower temperature range by ∼4 °C relative to that of heating. Evidently, the stress evolution behavior, including both magnitude and sign, in epitaxial VO_2 $(40\bar{2})_M/TiO_2$ (001) is completely different from that of polycrystalline $VO_2/SiO_2/Si$ (100) and epitaxial VO_2 $(020)_M$/sapphire (0001).

Fig. 5a shows thermal cycling of a 150 nm-thick VO_2 thin film at various heating and cooling rates, ranging from 5 °C /min to 20 °C /min. No significant differences exist among the curves at different thermal cycle rates. The results indicate the observed hysteresis is quite intrinsic to the film composition and is not nucleation limited at these rates (as oftentimes observed in case of nanobeams), nor is it limited by the temperature heterogeneity in the film [9]. Fig. 5b shows experiments in which we heated up a VO_2 thin film to different temperatures (72 °C, 74 °C, 78 °C, and 85 °C) at a rate of 1 °C /min. We then held the temperature constant at the maximum for 10 min, followed by cooling the samples to 50 °C at 1 °C /min. During the cooling period, all curves are relatively flat at first (indicative of hysteresis), after which the stress starts to decrease with various slopes. The (hysteretic) temperature range of the flat region during cooling increases as the maximum temperature increases, as does the slope of the stress-strain curve upon cooling below the flat (hysteretic) region. Fig. 5c shows 50 thermal cycles of a VO_2 thin film between 50 and 85 °C at a rate of 10 °C /min. The stress evolution during each cycle did not show any obvious changes after 50 thermal cycles. In Fig. 5d, we utilized FIB to examine a cross section of the cycled sample from Fig. 5c. The side view reveals no obvious mechanical damage either in terms of fracture or delamination, e.g., as compared with the damage produced during thermal cycling of the 1.63 µm-thick film shown Fig. 3a and b.

The electrical conductance and thermal hysteresis of VO_2 has been extensively studied using conductance measurements and differential scanning calorimetry during thermal cycling [1,7–10]. However, conductance and calorimetry results present a convolution of structural and electronic effects in this strongly electron correlated material. For instance, the latent heat differential measured by differential scanning calorimetry has (i) a lattice enthalpy component arising from the phonon-mediated $M_1 \rightarrow R$ (or reverse) phase transition initiated by V—V dimerization as well as (ii) a change in conduction entropy of charge carriers resulting from charge ordering/delocalization [52,53]. Our results (Figs. 4 and 5b) of the stress hysteresis measured during thermal cycling through multibeam optical sensor measurements provide an unequivocal view of just the lattice component of the phase transition.

We also implemented simultaneous measurements of mechanical stresses and electrical conductance during thermal cycling to study the influence of film orientation on the temperature sequence of the macroscopic IV response and overall stress response. We utilized two different samples, polycrystalline $VO_2/SiO_2/Si$ (100) and epitaxial VO_2 $(020)_M$/sapphire (0001) thin films, as they remain mechanically intact during thermal cycling but possess different in-plane and out-of-plane crystal orientation (by comparison VO_2 $(40\bar{2})_M/TiO_2$ (001) shows fracture even after film deposition, as indicated in Fig. 1). Upon careful inspection of Fig. 6a, the

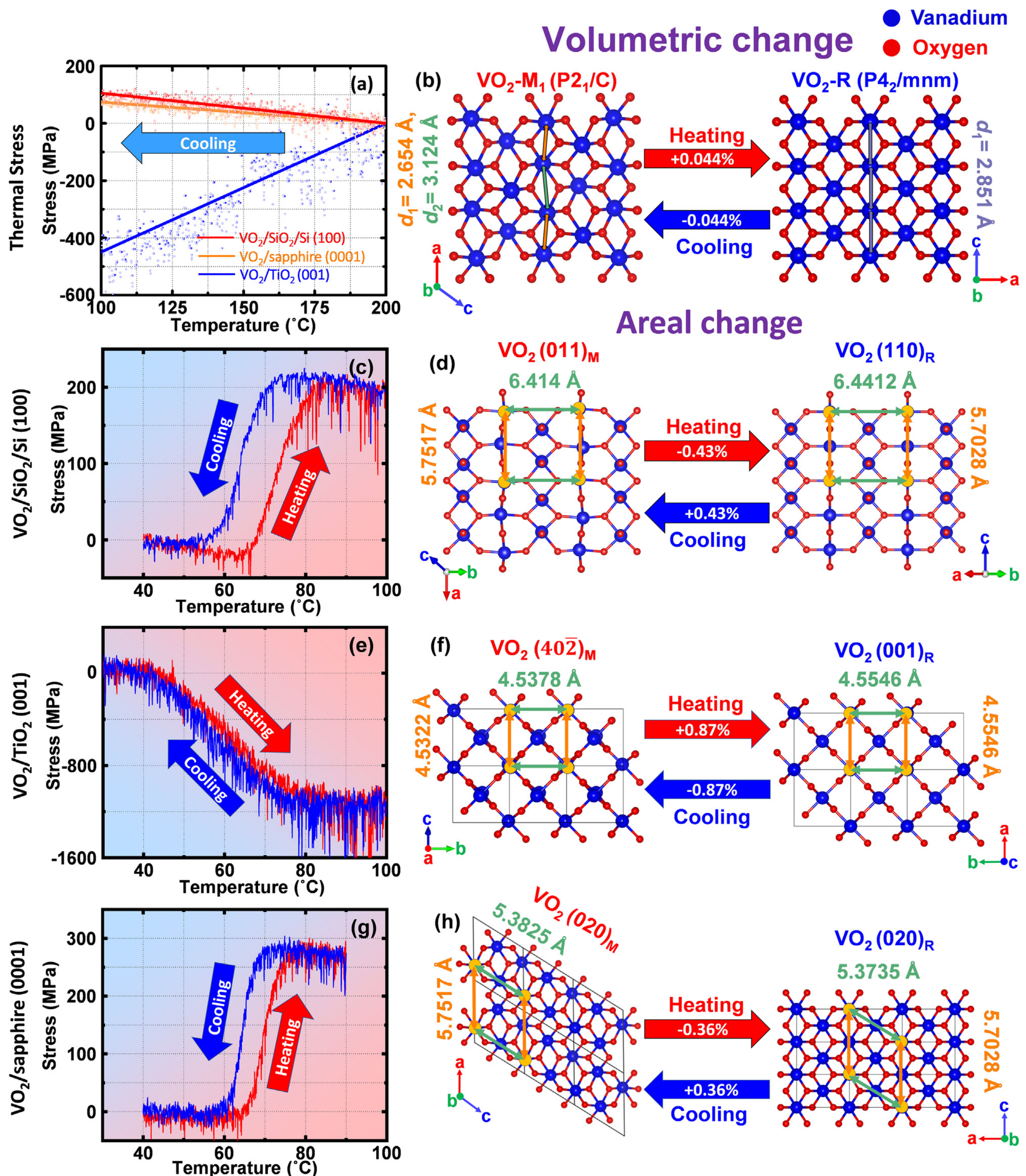

Fig. 4. (a) The stress evolution of VO_2 films during cooling from 200 °C to 100 °C at a cooling rate of 10ºC/min. (b) Volume changes between the VO_2-M and VO_2-R phases during the phase transformation. (c), (e), and (g): Evolution of stress in VO_2 thin films on various substrates during a thermal cycle. (d), (f), and (h): Areal changes in the VO_2 $(011)_M$, $(\bar{4}02)_M$, and $(020)_M$ planes and the corresponding VO_2 $(110)_R$, $(001)_R$, and $(020)_R$ planes on SiO_2/Si (100), TiO_2 (001), and sapphire (0001) during the phase transformation. These planes correspond to the primary (in the case of our highly textured polycrystalline VO_2 thin films) or exact (in the cases of our epitaxial VO_2 thin films) in-plane orientations of our VO_2 films, as indicated through XRD. The orange circles highlight atoms in a region of interest for discussion. The crystal structure of the VO_2_M is from reference [31] and the VO_2-R phase is from reference [32].

stress in polycrystalline VO_2 starts to change from relative compression to tension at ~65 °C, whereas the electrical conductance does not yet begin to significantly change at this point. By contrast, Fig. 5c shows that during the phase transformation of epitaxial VO_2 $(020)_M$/sapphire (0001) (from ~67 to 75 °C), the electrical conductance changes more quickly with temperature than does the mechanical stress, i.e., the macroscopic IV response appears to finish more quickly than does the overall stress response. In Fig. 6b and d, we plot the derivative of the curves in Fig. 6a and b to further highlight these points. During heating, Fig. 6b shows that the

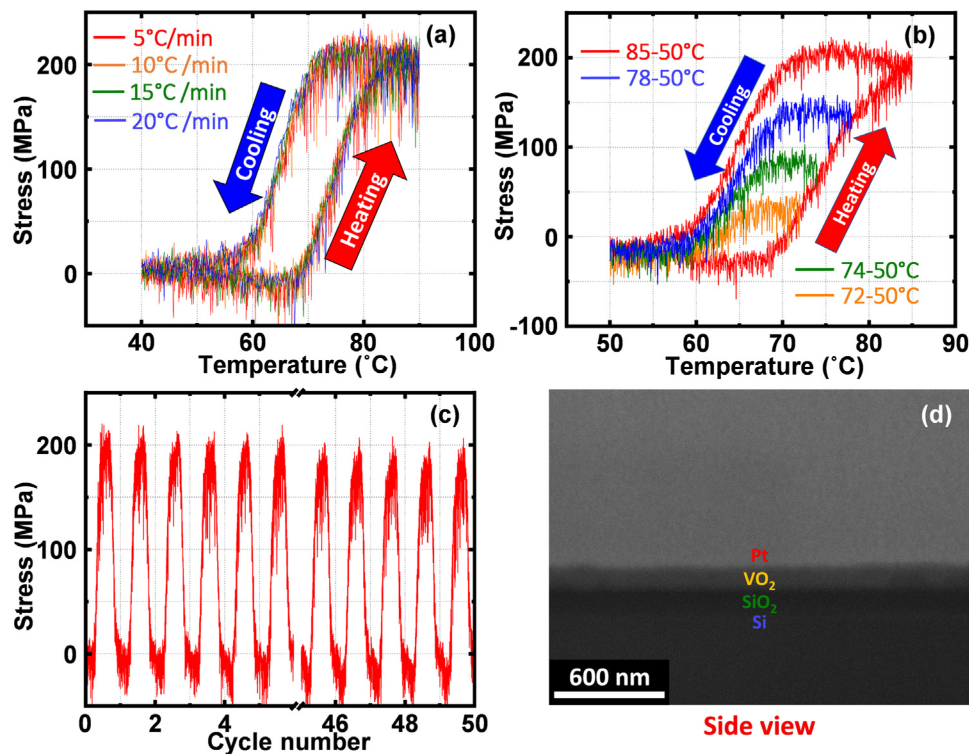

Fig. 5. (a) Stress evolution of a 150 nm-thick VO_2 film on SiO_2/Si (100) during thermal cycling from 40 °C to 90 °C at various heating/cooling rates. (b) Stress evolution upon heating and cooling to different temperatures (incomplete heating) at a heating/cooling rate of 1 °C /min. (c) Stress evolution during 50 thermal cycles. (d) Cross-sectional SEM image of the as-cycled sample from (c).

derivative of the mechanical stress of polycrystalline VO_2/SiO_2/Si (100) reaches a peak at a lower temperature than the corresponding derivative of the electrical conductance. By contrast, Fig. 6d shows that the derivative of the electrical conductance of epitaxial VO_2 $(020)_M$/sapphire (0001) reaches a peak at a lower temperature than the corresponding derivative of the stress. We tested three samples of each type of film, and the same trends were observed in all tests.

4. Discussion

4.1. Crystal structure analysis and its influence on stress development

Fig. 4b shows that, during heating through the phase transition, a volumetric expansion of VO_2 occurs with a reported value of 0.044% [21,22]. However, the XRD results (Fig. 1c) show that our 150 nm films sputtered on SiO_2/Si (100) are highly textured, with most of the in-plane crystal planes being $(011)_M$. Indeed, several other studies have demonstrated that deposition of VO_2 most commonly results in a textured film with the VO_2 $(011)_M$ planes being predominately parallel to the substrate [20,54–59], likely because the $(011)_M$ plane possesses the lowest surface energy in the VO_2 crystal system [60–62]. We calculated the in-plane areal change through the phase transformation by tracking the atoms in the representative region marked by the orange circles in Fig. 4d, f, and h. Fig. S5 provides calculation details. As shown in Fig. 4d, the a-axis in VO_2-M (denoted as the c-axis in VO_2-R) contracts by 0.85% upon transforming to VO_2-R, while the corresponding in-plane direction perpendicular to a-axis in VO_2-M (also in the plane of interest, as shown as the horizontal direction in Fig. 4d) expands by only 0.424%. In Fig. S6, we show another view of the VO_2 $(011)_M$ plane and calculation details for further clarity. Applying the same logic, we calculate the in-plane areal change of VO_2/TiO_2 (001) and VO_2/sapphire (0001) as shown in Fig. 6f and h. These simple structural analyses provide clear insight into these film systems. In particular, we predict that the stresses should be tensile and of a similar value in both VO_2/SiO_2/Si (100) and VO_2/sapphire (0001), whereas the stresses should be compressive and much larger in VO_2/TiO_2 (001) upon heating through the phase transformation. To reiterate, the stress we measured through the MOS technique represents the average in-plane stress. The expansion/contraction out of plane will not contribute to the stresses that develop in this film/substrate geometry. As such, this crystal structure analysis (Fig. 4d, f and h) explains our seeming stress evolution disparity measured in Fig. 4c, e and g, in which we observe the anisotropic behavior of the stress evolution during a thermal cycle.

This analysis highlights the importance of strategic texturation of films in its corresponding influence on stress evolution history that will develop during thermal cycling, which has key implications in practical devices. In terms of crystal structures of VO_2, the relative orientation in-plane and out-of-plane will govern whether tensile or compressive stresses build up in these constrained geometries, e.g., as are typical of multi-layered structures in devices. Delamination between VO_2 and surrounding layers may be driven by either compression or tension in the VO_2. Fracture of VO_2 itself will be driven by tensile stresses. As such, damage may be mitigated or prevented by strategically texturing film/layers of VO_2 in devices. We will elaborate on designing mechanically robust thin films that can survive repeated structural transformations in a later section.

4.2. The temperature evolution of metal-insulator transitions and structural phase transitions in VO_2 thin films

Fig. 6 shows that the overall macroscopic electrical response of the film appears shifted in temperature relative to the over-

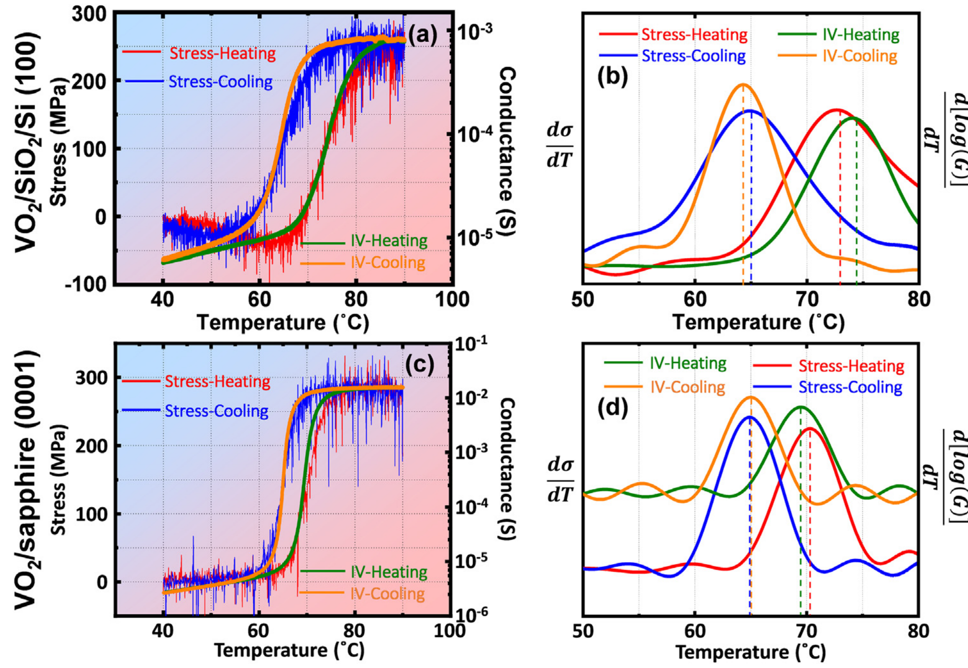

Fig. 6. (a) and (c): Simultaneous measurements of mechanical stress and electrical conductance of polycrystalline VO_2/SiO_2/Si (100) and epitaxial VO_2 $(020)_M$/sapphire (0001) during a thermal cycle. (b) and (d): Corresponding derivatives of stress and conductance with respect to the temperature of the data from (a) and (c).

all macroscopic stress response of the film. Both the macroscopic electrical resistivity and the overall film stress are proxies for the extent of phase transformation in the region of phase coexistence, but they have different nonlinear dependencies due to spatial heterogeneities during the metal-insulator transition. In literature studies of highly epitaxial films, VO_2 has shown alternative phase domains along the direction perpendicular to VO_2 $(001)_R$ direction, accompanied by a corresponding anisotropy in electronic transport [27,28]. Indeed, AFM phase mapping in Fig. S8e-S8h shows that our epitaxial films form some of these relatively long (high aspect ratio) conducting channels locally upon heating near the transition temperature. This process is conducive to more-readily creating a percolating network of electrical conductance (within the plane of the film). As such, even if a relatively small percentage of the VO_2-M has undergone a structural transition, the percolation of the electrical path would trigger a steeper slope of the conductance with temperature while heating through the transition. In polycrystalline textured VO_2 thin films, the in-plane directions are more randomly distributed than in epitaxial $VO_2(020)_M$/sapphire (0001), the latter of which exhibits 3 symmetrically equivalent rotational domains (which result in the superposition in the diffraction pattern with 6-fold symmetry). The residual stress acting on the c-axis of VO_2-R in the whole sample varies from grain to grain. Furthermore, the strain heterogeneity leads to local variation in the transition temperature. Thus, the grains subjected to compression on the c-axis (VO_2-R) undergo the phase transformation prior to the others. This type of behavior can lead to the observation from several groups of “metallic puddles” (VO_2-R) forming spatially during the phase transformation in polycrystalline VO_2 thin films [29,63]. We see a similar behavior in our polycrystalline films, as indicated by the circles in Fig. S8b. As this process is semi-randomly-distributed in a polycrystalline material, it is not as easy to create an in-plane conducting path until a relatively larger percentage of the volume has transformed.

4.3. Fracture analysis of polycrystalline VO_2 thin films: critical film thickness to avert failure

Fig. 3a and b show that our 1.63 µm-thick polycrystalline VO_2 thin films fracture after film fabrication and a thermal cycle. Our thinner polycrystalline VO_2 films (698 nm, 387 nm, and 150 nm) do not indicate any evidence of fracture as shown in Fig. 3c,d and Figs. S1 and S2. The nanoindentation and MOS studies provide two important mechanical properties (E_f and σ_f) that are required to predict the critical conditions for fracture of a thin film of polycrystalline VO_2 on a constraining substrate (or correspondingly of such a film surrounded by other materials in a device). For a given stress, σ_f, that develops in the film, there exists a critical film thickness, h_{cr}, below which growth of a pre-existing channel crack becomes energetically unfavorable. To determine the critical thickness, we adopt a fracture mechanics analysis from Beuth [64,65]:

$$h_{cr} = \frac{E_f \Gamma_f}{Z\left(1-\upsilon_f^2\right)\sigma_f^2} \tag{1}$$

where E_f is the elastic modulus of the film; Γ_f is the fracture energy of the film; υ_f is Poisson ratio of the film; σ_f is the stress in the film including both the residual stress from the fabrication process, σ_r, – which we measure through $\sin^2\psi$ method as shown in Fig. S9 – and the phase-transformation induced stress, σ_{trans}; and Z is a dimensionless factor that depends on the material properties of the film and the substrate, as well as the geometry of the crack. For a single channel crack through the thickness of a film, Z is given by

$$Z = \frac{1}{2}\pi g(\alpha, \beta) \tag{2}$$

where $g(\alpha, \beta)$ is a function of Dundurs parameters, α and β, which are defined as:

$$\alpha = \frac{\bar{E}_f - \bar{E}_s}{\bar{E}_f + \bar{E}_s}, \quad \beta = \frac{\mu_f(1-2\upsilon_s) - \mu_s\left(1-2\upsilon_f\right)}{2\mu_f(1-\upsilon_s) + 2\mu_s\left(1-\upsilon_f\right)} \tag{3}$$

where the $\bar{E}_i = \frac{E_i}{1-\upsilon_i^2}$ represent the plane-strain moduli, and the $\mu_i = \frac{E_i}{2(1+\upsilon_i)}$ represent the shear moduli. Eqs. (3) and (4).

For an estimate of the critical film thickness for fracture based on Eq. (1), we implement the material properties and the maximum tensile stresses in the polycrystalline VO_2 film developed during phase transformation that we measured in this study and representative values for the Poisson's ratio (which is relatively unimportant in the analysis) and the fracture energy for a brittle ceramic: $E_f = 224$ GPa, $\sigma_f = \sigma_r + \sigma_{trans} =$ 983 MPa + 225 MPa = 1208 MPa, $\nu_f \sim 0.2$, and $\Gamma_f \sim 10$ J/m^2 [65]. The value of the function g(α,β) was determined by interpolating the values reported by Beuth, which gives a value of g(α,β) = 1.34, and through Eq. (2) gives a value of $Z = 2.1$. Substituting these values into Eq. (1) gives a critical film thickness of $h_{cr} \sim 761$ nm, which agrees reasonably well with our experiments in that our 150 nm, 387 nm, and 698 nm films did not fracture, while our 1.63 µm films fractured.

Our analysis provides quantitative insight into averting fracture. First, Eq. (1) shows that decreasing the film thickness is an effective technique to avert fracture, as it reduces the crack driving force [65,66]. Additionally, it is important to note that the critical thickness value will be strongly influenced by the residual stress σ_r from fabrication, which in our case was measured to be nearly four times that of the stress induced by the phase transformation itself. As such, fabrication techniques that induce less residual stress (particularly less tensile residual stress) are highly desirable in preventing fracture. Reducing residual stresses may be accomplished by implementing substrates that are conducive to smaller deposition-induced stress (e.g., lattice matched epitaxial films) and implementing substrates that have similar coefficients of thermal expansion to that of the VO_2 film, as to minimize thermal stresses that arise in cooling down from the high-temperature deposition. Likewise, deposition techniques that occur at lower temperatures and/or subsequent annealing to remove/reduce residual stresses are likely beneficial.

Finally, we should note that in this study we did not explicitly study the effects of fatigue. We did determine that our relatively thin (150 nm) VO_2 films are resilient to several (50) cycles without any evidence of damage, as shown in Fig. 5. However, in real computing architectures, after many orders of magnitude more on/off cycles and the corresponding stresses that occur through the metal-insulator transition, VO_2 films may undergo damage from effects of fatigue. In other words, films may still eventually fracture even if thinner than the critical film thickness predicted from Eq. (1), which warrants future studies.

4.4. Fracture analysis of epitaxial VO_2 thin film

By extrapolating Fig. 4a from 200 to 600 °C and by assuming no further creep-type reactions occurred (VO_2 has a high melting point, such that the homologous temperature at 600 °C is T/T_m=0.39), in cooling from 600 to 100 °C in the sputtering chamber, the polycrystalline VO_2 films on Si would develop around +525 MPa, the epitaxial VO_2 on sapphire (0001) would develop around +375 MPa, and the epitaxial VO_2 on TiO_2 (001) would develop around −2.25 GPa. Combining these values with those produced in cooling through the phase transformation (Fig. 4c, e and g), the total stress in the system in cooling to 40 °C (for now neglecting the growth stress, which includes lattice mismatch between the film and the substrate and any intrinsic stress induced by film deposition itself) for $VO_2/SiO_2/Si$ (100), VO_2 $(020)_M$/sapphire (0001), and VO_2 $(40\bar{2})_M/TiO_2$ (001) would be approximately +325 MPa, +100 MPa, and −1100 MPa, respectively.

Fig. S3 shows that VO_2/TiO_2 (001) fractures, whereas VO_2/sapphire (0001) remains mechanically robust after fabrication and a thermal cycle. Further thermal cycling did not appear to increase the crack density of VO_2/TiO_2 (001), as indicated in Fig. S3. Regarding the origin of the cracks in VO_2/TiO_2 (001), it is informative to consider the entire history of the films. The films are first sputter deposited and annealed at 600°C, followed by cooling to room temperature through the phase transition. As such, there are three main sources of stress generation associated with synthesis:

(1) Deposition and post annealing-induced stresses (at 600 °C).

(2) Thermal stresses that arise from thermal mismatch between the film and substrate (from 600 to 100 °C), and

(3) Stresses associated with the metal-insulator transition (from 100 to 40 °C).

In the previous paragraph, we quantified the stresses associated with (2) and (3). For VO_2/TiO_2 (001), we extrapolated our MOS data to predict ∼−2250 MPa (compression) arising from thermal stresses in cooling from 600 to 100 °C, followed by an additional ∼+1100 MPa from the phase transition during cooling period. In total, these two sources produce around −1150 MPa compression in the film during this process. The large residual compression from the lattice mismatch between the film and substrate during cooling process may generate a wrinkled structure, as we indeed observed as displayed in Fig. S4 [37]. However, compressive stresses are not typically conducive to fracture. By comparison, the lattice mismatch between the VO_2 $(001)_R$ and TiO_2 (001) in principle would induce tension during deposition itself [32,67]. Moreover, during post-annealing, all the pre-existing flaws generated during sputter deposition can continue to (initiate and) propagate into larger cracks, as can be seen in Fig. 1e. As such, we surmise that the main origin of the tensile stresses that could lead to fracture of our VO_2/TiO_2 (001) stems from (1) the deposition and post-deposition-annealing-induced stresses, which is different from previous studies that suggest that the phase transformation itself induced fracture of their specimens[16,24]. Still, we should note that the films we fabricated here are at least five times thicker than those of Nagashima et al. and Krisponeit et al.'s work [16,24]. Additionally, differences exist between our studies and others based on the synthesis conditions, e.g., in terms of deposition times, post-deposition annealing times, temperatures, powers, gas flow rates, etc. In our studies, we did not have the capability to monitor crack formation during each step of the fabrication process (which includes cooling down through the MIT). Still, based on our measurements, we expect that much (if not all) of the cracking was associated with deposition and annealing itself. We should emphasize that it is possible that under different synthesis conditions (e.g., in other studies), fracture may not occur from deposition and post-deposition-annealing but instead from another process (such as the MIT itself generating large enough tensile stresses to induce fracture). Regardless, our observations underscore the importance of the stresses generated during the deposition process itself.

Our analysis above provides the root cause of the fracture behavior of epitaxial VO_2/TiO_2 (001). To prevent fracture, as we mentioned in the last section, Eq. (1) indicates that decreasing film thickness could effectively reduce the crack driving force. Indeed, Nagashima found that thin films of VO_2/TiO_2 (001) less than 15 nm in thickness maintain mechanically integrity. Additionally, adding an appropriately designed buffer layer between the film and substrate may effectively decrease the lattice mismatch between the film and substrate, thereby reducing stresses and thus propensity for fracture. Furthermore, even if the transition temperature would be strongly shifted by the presence of the lattice mismatch between the film and the substrates, misfit dislocations can readily occur in even quite thin films. These misfit dislocations can induce adverse effect on the electronic performance of the semiconductor materials by serving as recombination centers that diminish

carrier density in devices [1,18,37]. As such, in order to achieve a high transition temperature to meet the needs of neuromorphic computing chips and also maintain a low residual strain inside the film (a high residual stress may induce a large misfit dislocation density), we recommended adopting a strategy of alloying the VO_2 films with other elements [68]. Lastly, implementing substrates that possess similar thermal expansion coefficients to the films would minimize the thermal stresses that arise in cooling down from the high-temperature deposition, which in turn could decrease the extent of the wrinkling due to the significant compression developed during cooling.

5. Conclusions

In this work, we have performed systematic mechanical characterization of sputter-deposited polycrystalline and epitaxial VO_2 thin films. Significant anisotropic stresses arose during thermal cycling of VO_2 thin films due to its metal-insulator phase transition. Despite VO_2 exhibiting overall volume expansion upon heating through this transition, our polycrystalline VO_2 thin films developed tensile stresses when heating through the phase transformation. We attribute this seeming contradiction to the highly textured nature of our sputter-deposited polycrystalline thin films, which leads to in-plane areal contraction through the phase transformation. Also, our epitaxial VO_2 films on sapphire (0001) developed tension whereas our epitaxial VO_2 films on TiO_2 (001) developed compression during heating through the phase transformation. We again attribute these disparities to the anisotropic deformation during the phase transformation. These observations highlight the importance of the strategic texturation of VO_2 films in its corresponding influence on stresses that develop during operation. In terms of mechanical damage, combining our measurements of the elastic modulus and the stresses developed during the deposition and subsequent thermal cycling of polycrystalline VO_2 thin films, we predicted a critical film thickness for our polycrystalline VO_2 films of 761 nm, below which we do not expect fracture. This prediction was corroborated by experiments and highlights a key design parameter to mitigate damage in practical devices of VO_2. Additionally, by analyzing the stress evolution history during the entire synthesis process, we concluded that epitaxial VO_2/TiO_2 (001) films fracture during sputter deposition itself. We also implemented a technique to perform simultaneous measurements of mechanical stresses and electrical conductance during a thermal cycle to study the influence of film orientation on the temperature sequence of macroscopic electrical response and overall stress response. We found that the macroscopic electrical response slightly precedes the overall stress response in polycrystalline $VO_2/SiO_2/Si$ (100), whereas the overall stress response slightly precedes the macroscopic electrical response in epitaxial VO_2 $(020)_M$/sapphire (0001). We attribute this observation to spatial heterogeneities during the phase transformation, which results in distinct (local) phase separation behavior and thus distinct electrical percolation paths.

Declaration of Competing Interest

The authors declare that they have no known competing financial interests or personal relationships that could have appeared to influence the work reported in this paper.

Acknowledgments

Y. Zhang, D. Zhao, P. Shamberger, K. Xie, and M. Pharr acknowledge funding from the X-Grants Program: A President's Excellence Fund at Texas A&M University. C. D. Fincher and R. Gurrola acknowledge support from the National Science Foundation Graduate Research Fellowship. S. Banerjee acknowledges support from the Welch Foundation under award #A-1978–20190330. We also acknowledge support from the Materials Characterization Facility (MCF) at Texas A&M University. We thank Baiyu Zhang, Xiaofeng Qian, and Timothy Brown for a number of useful discussions pertaining to this work.

Supplementary materials

Supplementary material associated with this article can be found, in the online version, at doi:10.1016/j.actamat.2022.118478.

References

[1] J. Jian, et al., Continuous tuning of phase transition temperature in VO_2 thin films on c-cut sapphire substrates via strain variation, ACS Appl. Mater. Interfaces 9 (2017) 5319–5327.
[2] H. Clarke, et al., Nucleation-controlled hysteresis in unstrained hydrothermal VO_2 particles, Phys. Rev. Mater. 2 (2018) 1–8.
[3] J.L. Andrews, D.A. Santos, M. Meyyappan, R.S. Williams, S. Banerjee, Building brain-inspired logic circuits from dynamically switchable transition-metal oxides, Trends Chem. 1 (2019) 711–726.
[4] J.H. Park, et al., Measurement of a solid-state triple point at the metal-insulator transition in VO_2, Nature 500 (2013) 431–434.
[5] J. Co, et al., Extended mapping and exploration of the vanadium dioxide stress-temperature phase diagram, Nano Lett. 10 (2010) 2667–2673.
[6] W. Yi, et al., Biological plausibility and stochasticity in scalable VO_2 active memristor neurons, Nat. Commun. 9 (2018).
[7] J. Jian, et al., Broad range tuning of phase transition property in VO_2 through metal-ceramic nanocomposite design, Adv. Funct. Mater. 1903690 (2019) 1–12.
[8] D.G. Sellers, et al., Atomic hourglass and thermometer based on diffusion of a mobile dopant in VO_2, J. Am. Chem. Soc. 142 (2020) 15513–15526.
[9] E.J. Braham, et al., Modulating the hysteresis of an electronic transition: launching alternative transformation pathways in the metal-insulator transition of vanadium(IV) oxide, Chem. Mater. 30 (2018) 214–224.
[10] T.E.G. Alivio, et al., Postsynthetic route for modifying the metal-insulator transition of VO_2 by interstitial dopant incorporation, Chem. Mater. 29 (2017) 5401–5412.
[11] T. Yajima, Y. Ninomiya, T. Nishimura, A. Toriumi, Drastic change in electronic domain structures via strong elastic coupling in VO_2 films, Phys. Rev. B Condens. Matter Mater. Phys. 91 (2015) 1–6.
[12] K. Kawatani, T. Kanki, H. Tanaka, Formation mechanism of a microscale domain and effect on transport properties in strained VO_2 thin films on TiO_2(001), Phys. Rev. B Condens. Matter Mater. Phys. 90 (2014) 1–5.
[13] E. Abreu, et al., THz spectroscopy of VO_2 epitaxial films: controlling the anisotropic properties through strain engineering, New J. Phys. 14 (2012) 083026.
[14] M. Liu, et al., Phase transition in bulk single crystals and thin films of VO_2 by nanoscale infrared spectroscopy and imaging, Phys. Rev. B Condens. Matter Mater. Phys. 91 (2015) 245155.
[15] L. Rodríguez, et al., Self-pixelation through fracture in VO_2 thin films, ACS Appl. Electron. Mater. 2 (2020) 1433–1439.
[16] K. Nagashima, T. Yanagida, H. Tanaka, T Kawai, Stress relaxation effect on transport properties of strained vanadium dioxide epitaxial thin films, Phys. Rev. B Condens. Matter Mater. Phys. 74 (2006) 13–16.
[17] H. Paik, et al., Transport properties of ultra-thin VO_2 films on (001) TiO_2 grown by reactive molecular-beam epitaxy, Appl. Phys. Lett. 107 (2015) 1–6.
[18] Y. Muraoka, Z. Hiroi, Metal-insulator transition of VO_2 thin films grown on TiO_2 (001) and (110) substrates, Appl. Phys. Lett. 80 (2002) 583–585.
[19] B. Viswanath, C. Ko, S. Ramanathan, Thermoelastic switching with controlled actuation in VO2 thin films, Scr. Mater. 64 (2011) 490–493.
[20] V. Balakrishnan, C. Ko, S. Ramanathan, *In situ* studies on twinning and cracking proximal to insulator-metal transition in self-supported VO_2/Si_3N_4 membranes, J. Mater. Res. 27 (2012) 1476–1481.
[21] T. Kawakubo, T. Nakagawa, Phase transition in VO_2, J. Phys. Soc. Jpn. 19 (1964) 517–519.
[22] D. Kucharczyk, T. Niklewski, Accurate X-ray determination of the lattice parameters and the thermal expansion coefficients of vo_2 near the transition temperature, J. Appl. Cryst. 12 (1979) 370–373.
[23] F. Sandiumenge, et al., Metallic diluted dimerization in VO_2 tweeds, Adv. Mater. 33 (2021) 1–8.
[24] J.O. Krisponeit, et al., The morphology of VO_2/TiO_2(001): terraces, facets, and cracks, Sci. Rep. 10 (2020) 1–8.
[25] Y. Yang, et al., Thickness effects on the epitaxial strain states and phase transformations in (001)-VO_2/TiO_2 thin films, J. Appl. Phys. 125 (2019) 082508.
[26] M. Liu, et al., Symmetry breaking and geometric confinement in VO_2: results from a three-dimensional infrared nano-imaging, Appl. Phys. Lett. 104 (2014) 1–6.
[27] M.K. Liu, et al., Anisotropic electronic state via spontaneous phase separation in strained vanadium dioxide films, Phys. Rev. Lett. 111 (2013) 1–5.
[28] M. Liu, A.J. Sternbach, D.N Basov, Nanoscale electrodynamics of strongly correlated quantum materials, Rep. Prog. Phys. 80 (2017) 14501.

[29] M.M. Qazilbash, et al., Mott transition in VO_2 revealed by infrared spectroscopy and nano-imaging, Science 318 (2007) 1750–1753 (80-.).
[30] K. Momma, F. Izumi, VESTA 3 for three-dimensional visualization of crystal, volumetric and morphology data, J. Appl. Crystallogr. 44 (2011) 1272–1276.
[31] M. John, P.K. Longo, A refinement of the structure of VO_2, Acta Chem. Scand. 24 (1970) 420–426.
[32] D.B. McWhan, M. Marezio, J.P. Remeika, P.D. Dernier, X-ray diffraction study of metallic VO_2, Phys. Rev. B 10 (1974) 490–495.
[33] Y. Zhang, et al., *In-situ* measurements of stress evolution in composite sulfur cathodes, Energy Storage Mater. 16 (2018) 491–497.
[34] Y. Zhang, Y. Luo, C. Fincher, S. Banerjee, M. Pharr, Chemo-mechanical degradation in V2O5 thin film cathodes of Li-ion batteries during electrochemical cycling, J. Mater. Chem. A 7 (2019) 23922–23930.
[35] Y. Zhang, C. Fincher, S. McProuty, M. Pharr, In-operando imaging of polysulfide catholytes for Li–S batteries and implications for kinetics and mechanical stability, J. Power Sources 434 (2019) 226727.
[36] M.A. Hopcroft, W.D. Nix, T.W Kenny, What is the Young's modulus of silicon? J. Microelectromech. Syst. 19 (2010) 229–238.
[37] Freund, L.B. & Suresh, S. (2004). Thin film materials: stress, defect formation and surface evolution. Cambridge university press.
[38] G.C.A.M. Janssen, M.M. Abdalla, F. van Keulen, B.R. Pujada, B. van Venrooy, Celebrating the 100th anniversary of the Stoney equation for film stress: developments from polycrystalline steel strips to single crystal silicon wafers, Thin Solid Films 517 (2009) 1858–1867.
[39] F. Huang, M.L. Weaver, Effective biaxial modulus of ideally (hkl)-fiber-textured hexagonal, tetragonal, and orthorhombic films, J. Appl. Phys. 100 (2006) 093523.
[40] W.G. Mayer, E.A Hiedemann, Optical methods for the ultrasonic determination of the elastic constants of sapphire, J. Acoust. Soc. Am. 30 (1958) 756–760.
[41] W.G. Mayer, E.A Hiedemann, Corrected values of the elastic moduli of sapphire, J. Acoust. Soc. Am. 32 (1960) 1699–1700.
[42] D.G. Isaak, J.D. Carnes, O.L. Anderson, H. Cynn, E. Hake, Elasticity of TiO_2 rutile to 1800K, Phys. Chem. Miner. 26 (1998) 31–43.
[43] D.H. Chung, W.R. Buessem, The voigt-reuss-hill (VRH) approximation and the elastic moduli of polycrystalline ZnO, TiO_2 (rutile), and α-Al_2O_3, J. Appl. Phys. 39 (1968) 2777–2782.
[44] V.A. Sethuraman, M.J. Chon, M. Shimshak, V. Srinivasan, P.R. Guduru, *In situ* measurements of stress evolution in silicon thin films during electrochemical lithiation and delithiation, J. Power Sources 195 (2010) 5062–5066.
[45] W.C. Oliver, G.M Pharr, An improved technique for determining hardness and elastic modulus using load and displacement sensing indentation experiments, J. Mater. Res. 7 (1992) 1564–1583.
[46] J. Hay, B Crawford, Measuring substrate-independent modulus of thin films, J. Mater. Res. 26 (2011) 727–738.
[47] X. Chen, J.J Vlassak, Numerical study on the measurement of thin film mechanical properties by means of nanoindentation, J. Mater. Res. 16 (2001) 2974–2982.
[48] J.D. Budai, et al., Metallization of vanadium dioxide driven by large phonon entropy, Nature 515 (2014) 535–539.
[49] R.K. Kirby, Thermal expansion of rutile from 100 to 700K, J. Res. Natl. Bur. Stand. Sect. A Phys. Chem. 71A (1967) 363.
[50] M. Leszczynski, et al., Thermal expansion of gallium nitride, J. Appl. Phys. 76 (1994) 4909–4911.
[51] H. Watanabe, N. Yamada, M. Okaji, Linear thermal expansion coefficient of silicon from 293 to 1000K, Int. J. Thermophys. 25 (2004) 221–236.
[52] C.N. Berglund, H.J. Guggenheim, Electronic properties of VO_2 near the semiconductor-metal transition, Phys. Rev. 185 (1969) 1022–1033.
[53] A.V. Salker, K. Seshan, Phase transition behaviour of VO_2, Phys. Status Solidi A 75 (1983) K37–K40.
[54] C. Huang, Z. Zhang, S. Ramanathan, D. Weinstein, VO_2 phase-transition-based vertical MEMS microactuators, IEEE Trans. Electron Devices 66 (2019) 4380–4386.
[55] B. Rajeswaran, L.R. Viannie, K. Rajanna, G.R. Jayanth, A.M. Umarji, Phase transition induced micromechanical actuation in VO_2 coated cantilever, J. Appl. Phys. 124 (2018) 074502.
[56] T. Lin, L. Wang, X. Wang, Y. Zhang, Y. Yu, Influence of lattice distortion on phase transition properties of polycrystalline VO_2 thin film, Appl. Surf. Sci. 379 (2016) 179–185.
[57] Y. Yang, et al., Transmittance change with thickness for polycrystalline VO_2 films deposited at room temperature, J. Alloy. Compd. 791 (2019) 648–654.
[58] K. Zhang, et al., Synthesis of VO_2 thin films by atomic layer deposition with TEMAV as precursor, ECS Trans. 50 (2013) 175–182.
[59] Z. Yang, C. Ko, S. Ramanathan, Metal-insulator transition characteristics of VO_2 thin films grown on Ge(100) single crystals, J. Appl. Phys. 108 (2010) 073708.
[60] B.S. Guiton, Q. Gu, A.L. Prieto, M.S. Gudiksen, H Park, Single-crystalline vanadium dioxide nanowires with rectangular cross sections, J. Am. Chem. Soc. 127 (2005) 498–499.
[61] A. Haras, M. Witko, D.R. Salahub, K. Hermann, R. Tokarz, Electronic properties of the VO_2 (011) surface: density functional cluster calculations, Surf. Sci. 491 (2001) 77–87.
[62] J.I. Sohn, et al., Direct observation of the structural component of the metal-insulator phase transition and growth habits of epitaxially grown VO_2 nanowires, Nano Lett. 7 (2007) 1570–1574.
[63] H. Kim, et al., Direct observation of the M_2 phase with its Mott transition in a VO_2 film, Appl. Phys. Lett. 109 (2016) 233104.
[64] J.L. Beuth, Cracking of thin bonded films in residual tension, Int. J. Solids Struct. 29 (1992) 1657–1675.
[65] M. Pharr, Z. Suo, J.J Vlassak, Measurements of the fracture energy of lithiated silicon electrodes of Li-Ion batteries, Nano Lett. 13 (2013) 5570–5577.
[66] G.R. Hardin, Y. Zhang, C.D. Fincher, M. Pharr, Interfacial Fracture of Nanowire Electrodes of Lithium-Ion Batteries, Jom 69 (2017) 1519–1523.
[67] S.C. Abrahams, J.L. Bernstein, Rutile: normal probability plot analysis and accurate measurement of crystal structure, J. Chem. Phys. 55 (1971) 3300–3307.
[68] P. Schofield, et al., Decoupling the metal–insulator transition temperature and hysteresis of VO_2 using Ge alloying and oxygen vacancies, Chem. Commun. 58 (2022) 6586–6589.